AN EFFICIENT ROTATION-FREE TRIANGLE FOR DRAPE/CLOTH SIMULATIONS -PART I: MODEL IMPROVEMENT, DYNAMIC SIMULATION AND ADAPTIVE REMESHING*

K.Y. SZE† and Y.X. ZHOU

Department of Mechanical Engineering, The University of Hong Kong
Pokfulam, Hong Kong, P.R. China
kysze@hku.hk

This series of two papers aim to improve the rotation-free (RF) triangle model previously developed by the authors and apply it for drape/cloth simulations. To avoid a previously un-observed drawback, the membrane strain obtained from the three-node displacement interpolation is replaced by the one obtained from the six-node interpolation. Dynamic simulations are made possible by explicit time integration. Instead of using dense structural meshes, the quality of draped patterns is improved by introducing a global adaptive remeshing. The works in this paper provide important and necessary techniques for practical applications of the RF triangle in the drape simulation. In part II, other techniques including collision handling and garment construction are further discussed and some practical applications of garments on still and moving human body model would be presented.

Keywords: rotation-free; triangle; drape/cloth simulations; adaptive remeshing.

1. Introduction

The drape/cloth simulation can be an efficient tool to meet new challenges of the apparel industry such as the development of electronic markets, customization and reduction in lead times [Zulch *et al.*, 2011]. It can also enhance the reality of the animated movies [Choi and Ko, 2005]. Nevertheless, practical applications of physical-based simulations are still very limited [Smith Micro Software Inc, 2012].

Physical-based computational models in the drape/cloth simulation can broadly be divided into skeletal and non-skeletal models. Mass-spring models (or also called as particle models), e.g., [Breen *et al.*, 1994; Provot, 1995; Chen *et al.*, 2001; Zhang and Yuen, 2001; Sze and Liu, 2005; Villard and Boeouchaki, 2005; Ji *et al.*, 2006], are the most popularly used skeletal models. In these models, the deformation energy of the fabrics, including tensile, bending, trellising or even yarn repelling energies, is derived from various springs connecting the particles. The critical shortcoming of skeletal models is that they are stringent on the particle distribution which leads to the laborious treatment for oblique and curved boundaries [Chen *et al.*, 2001; Sze and Liu, 2005; Villard and

---

Boeouchaki, 2005]. The most commonly used non-skeletal models in the drape/cloth simulation are the shell finite element models, see [Gan *et al.*, 1995; Kang and Yu, 1995; Eischen *et al.*, 1996; Tan *et al.*, 1999; Gong *et al.*, 2001], among others. However, the applications of shell finite element models in the drape/cloth simulation are not as successful as in structural analyses, and most previous attempts are rather restricted to problems with shallow folds/wrinkles. A possible reason is that nodes of shell element models carry not only translational but also rotational dofs which often require special treatment for the finite rotation analysis. Solid-shell element model which possesses no rotational dofs has also been applied to the drape simulation [Sze and Liu, 2007]. Unfortunately, a spurious zero energy mode in which the lower and upper faces of the element interpenetrate each other is encountered as a result of the employed assumed natural shear and transverse strain schemes for locking alleviation. When the free hanging length of the fabric is long, the solution often fails to converge.

The rotation-free (RF) element is a family of thin plate/shell elements in which there are only 3 translational dofs per director and rotational dofs are not employed. Compared with the degenerated- and solid-shell elements, RF models possess the following advantages: their stiffness matrices are better conditioned, they converge more readily in nonlinear analyses and the related contact treatment is also simpler [Benson *et al.*, 2011; Flores and Onate, 2011]. Although they may not be as accurate as the degenerated- and solid-shell elements under unstructured meshes [Gardsback and Tibert, 2007], they appear to be good candidates for large displacement analyses of very thin plate/shell problems and drape/cloth simulations [Flores and Onate, 2011; Zhou and Sze, 2012].

There are quite a number of RF models in the literature. They include the RF models based on interpolation [Phaal and Calladine, 1992a; Liu and Sze, 2009], hinge-angle [Phaal and Calladine, 1992b; Guo *et al.*, 2002; Sabourin and Brunet, 2006], subdivision of surface [Cirak and Ortiz, 2001], the concept of the finite volume method [Onate and Zarate, 2000; Flores and Onate, 2005, 2011] and meshfree method [Sze *et al.*, 2004; Cui *et al.*, 2011]. Recently, the authors have developed a RF triangle and applied it to the drape simulation [Zhou and Sze, 2012]. Compared with other exiting RF models, it is very simple but its accuracy remains competitive. As CST based on the three-node displacement interpolation is employed to take the membrane energy into account, the RF triangle will be referred to as RFT3 hereafter. Using a corotational approach, the tangential bending stiffness matrix of the triangle can be approximated by a constant matrix which greatly simplifies the geometrical nonlinear analyses. However, [Zhou and Sze, 2012] is restricted to static drape simulation whilst drape/cloth simulation is at the crossroad of many technologies [Volino and Cordier, 2004] related to computer graphics, textile engineering, computational mechanics, etc.

In this series of two papers, RFT3 would be improved and integrated with other technologies. The ultimate goal is to simulate cloth on still and moving human body model. For the present paper, RFT3 is reviewed and the scheme for the explicit dynamic analysis is presented in Section 2. In Section 3, the membrane strain in RFT3 obtained from the three-node interpolation is replaced by the one obtained from the six-node interpolation so as to avoid a drawback which sometimes leads to non-physical sharp

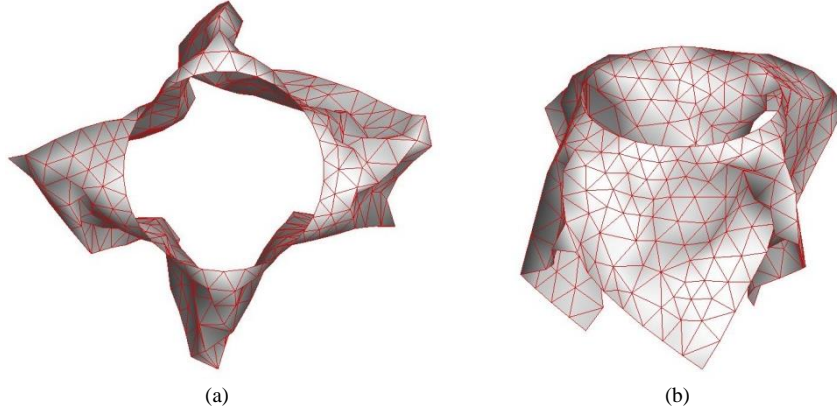<div align="center">(a)   (b)</div>

Fig. 1. (a) Top and (b) isometric views of a 50×50 cm fabric on a Ø20 cm pedestal predicted by the previous RF triangle using 371 nodes [Zhou and Sze, 2012].

folds, see Fig. 1, for instance. The same practice was also employed by Flores & Onãte [2005] for, however, improving the accuracy of their RF model. In Section 4, some drape examples are presented. Section 5 introduces an adaptive remeshing scheme which enables finer details of folds/wrinkles be resolved with a relatively smaller number of nodes. Further numerical examples follow in Section 6.

2. Review of the rotation-free triangle

In this section, RFT3 previously formulated for static problems [Zhou and Sze, 2012] is briefly reviewed and the explicit time integration scheme to be employed is discussed.

2.1. *Linear bending formulation*

The RF triangle can consider problem domains with initial curvatures. As cloth is mostly made of flat fabrics, the review here will be restricted to problem domains which are initially flat. Consider the six-node coplanar element patch 1-2-3-4-5-6. The local inplane coordinates are (x,y). The displacement transverse to the x-y-plane can be expressed as:

$$w = c_1 + c_2 x + c_3 y + c_4 x^2 / 2 + c_5 y^2 / 2 + c_6 xy / 2 \tag{1}$$

The interpolation requirement leads to:

$$\begin{Bmatrix} w_1 \\ \vdots \\ w_6 \end{Bmatrix} = \begin{bmatrix} 1 & x_1 & y_1 & x_1^2/2 & y_1^2/2 & x_1 y_1/2 \\ \vdots & \vdots & \vdots & \vdots & \vdots & \vdots \\ 1 & x_6 & y_6 & x_6^2/2 & y_6^2/2 & x_6 y_6/2 \end{bmatrix} \begin{Bmatrix} c_1 \\ \vdots \\ c_6 \end{Bmatrix} = \mathbf{C} \begin{Bmatrix} c_1 \\ \vdots \\ c_6 \end{Bmatrix} \tag{2}$$

where (x_i, y_i) are the (x, y) coordinates of the i-th node and $\mathbf{C}$ is self-defined. Under the small displacement assumption, the curvature can be derived as:

4

$$\boldsymbol{\kappa} = \begin{Bmatrix} \kappa_x \\ \kappa_y \\ \kappa_{xy} \end{Bmatrix} = - \begin{Bmatrix} w,_{xy} \\ w,_{yy} \\ 2w,_{xy} \end{Bmatrix} = - \begin{Bmatrix} c_4 \\ c_5 \\ c_6 \end{Bmatrix} = -\mathbf{L} \begin{Bmatrix} w_1 \\ \vdots \\ w_6 \end{Bmatrix} \tag{3}$$

in which $\mathbf{L}$ is the lower half of $\mathbf{C}^{-1}$. With the constant curvature obtained from the last equation taken to be the curvature of the RF triangle 4-5-6, the elastic bending energy stored in the triangle is:

$$E^b = \frac{A}{2} \begin{Bmatrix} \kappa_x \\ \kappa_y \\ \kappa_{xy} \end{Bmatrix}^T \mathbf{D}^b \begin{Bmatrix} \kappa_x \\ \kappa_y \\ \kappa_{xy} \end{Bmatrix} = \frac{A}{2} \begin{Bmatrix} w_1 \\ \vdots \\ w_6 \end{Bmatrix}^T \mathbf{L}^T \mathbf{D}^b \mathbf{L} \begin{Bmatrix} w_1 \\ \vdots \\ w_6 \end{Bmatrix} \tag{4}$$

in which A is the area of the triangle and where $\mathbf{D}^b = [D_{ij}^b]$ is the bending rigidity matrix. Based on the bending energy, the linear static plate bending problem can be solved by minimizing the total potential.

2.2. *Geometrical nonlinear bending formulation*

The corotational approach has been employed to extend the bending formulation to the large displacement, large rotation but small strain analyses [Zhou and Sze, 2012]. With reference to Fig. 2, the initial configuration 1-2-3-4-5-6 undergoes displacement $\mathbf{U}$ and assumes the deformed configuration 1'-2'-3'-4'-5'-6'. Meanwhile, a fictitious rigid body displacement $\mathbf{U}^C$ can be defined such that it brings 1-2-3-4-5-6 to the corotational configuration 1^C-2^C-3^C-4^C-5'-6^C such that 5', 6^C and 6' are collinear whilst 4^C-5'-6^C and 4'-5'-6' are coplanar. The corotational frame (x,y,z) is defined with the corotational configuration lies on the x-y plane and the origin taken rather arbitrary at node 5'. With $\mathbf{n}$ denoting the unit vector along z, the transverse displacement w along the z-axis from the corotational to the deformed configuration is:

$$w = \mathbf{n}^T (\mathbf{U} - \mathbf{U}^C) \tag{5}$$

Since $\mathbf{U}^C$ is a rigid body displacement, it is trivial that

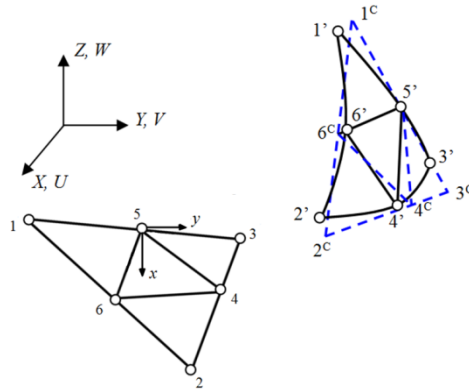$$\mathbf{U},_{pq}^C = \mathbf{0} \quad \text{for } p, q = x, y. \tag{6}$$

Fig. 2. An initially flat element patch. 1-2-3-4-5-6, 1^C-2^C-3^C-4^C-5'-6^C, and 1'-2'-3'-4'-5'-6' are the initial, corotational and deformed configurations, respectively.

From Eq.(5), Eq.(6) and the small-strain-small-curvature assumption, the curvature $\boldsymbol{\kappa}$ and the bending energy E^b for triangle 4-5-6 can be approximated as:

$$\boldsymbol{\kappa} = \begin{Bmatrix} \kappa_{xx} \\ \kappa_{yy} \\ \kappa_{xy} \end{Bmatrix} = \begin{Bmatrix} w,_{xx} \\ w,_{yy} \\ 2w,_{xy} \end{Bmatrix} = \begin{Bmatrix} \mathbf{n}^T(\mathbf{U}-\mathbf{U}^C),_{xx} \\ \mathbf{n}^T(\mathbf{U}-\mathbf{U}^C),_{yy} \\ 2\mathbf{n}^T(\mathbf{U}-\mathbf{U}^C),_{xy} \end{Bmatrix} = \begin{Bmatrix} \mathbf{n}^T\mathbf{U},_{xx} \\ \mathbf{n}^T\mathbf{U},_{yy} \\ 2\mathbf{n}^T\mathbf{U},_{xy} \end{Bmatrix}. \tag{7}$$

and

$$E^b = \frac{A}{2}\boldsymbol{\kappa}^T\mathbf{D}^b\boldsymbol{\kappa} = \frac{A}{2}\begin{Bmatrix} \mathbf{n}^T\mathbf{U},_{xx} \\ \mathbf{n}^T\mathbf{U},_{yy} \\ 2\mathbf{n}^T\mathbf{U},_{xy} \end{Bmatrix}^T \mathbf{D}^b \begin{Bmatrix} \mathbf{n}^T\mathbf{U},_{xx} \\ \mathbf{n}^T\mathbf{U},_{yy} \\ 2\mathbf{n}^T\mathbf{U},_{xy} \end{Bmatrix} = \frac{A}{2}\begin{Bmatrix} \mathbf{U},_{xx} \\ \mathbf{U},_{yy} \\ 2\mathbf{U},_{xy} \end{Bmatrix}^T \mathbf{D}^b \begin{Bmatrix} \mathbf{n}\mathbf{n}^T\mathbf{U},_{xx} \\ \mathbf{n}\mathbf{n}^T\mathbf{U},_{yy} \\ 2\mathbf{n}\mathbf{n}^T\mathbf{U},_{xy} \end{Bmatrix} \tag{8}$$

The small-strain-small-curvature assumption further allows one to write

$$\mathbf{U}-\mathbf{U}^C \simeq \mathbf{n}w = \mathbf{n}\mathbf{n}^T(\mathbf{U}-\mathbf{U}^C). \tag{9}$$

in which Eq.(5) has been invoked. From Eq.(6) and the fact that $\mathbf{n}$ does not vary with (x,y), differentiation of Eq.(9) leads to:

$$\mathbf{U},_{pq} \simeq \mathbf{n}\mathbf{n}^T\mathbf{U},_{pq} \qquad \text{for } p, q = x, y. \tag{10}$$

By substituting the last equation into Eq.(8), the bending energy is simplified as:

$$E^b = \frac{A}{2}\begin{Bmatrix} \mathbf{U},_{xx} \\ \mathbf{U},_{yy} \\ 2\mathbf{U},_{xy} \end{Bmatrix}^T \mathbf{D}^b \begin{Bmatrix} \mathbf{U},_{xx} \\ \mathbf{U},_{yy} \\ 2\mathbf{U},_{xy} \end{Bmatrix}. \tag{11}$$

By interpolating $\mathbf{U}$ with respect to (x,y) in the same way as in Eqs.(1)-(3),

$$\begin{Bmatrix} \mathbf{U},_{xx} \\ \mathbf{U},_{yy} \\ 2\mathbf{U},_{xy} \end{Bmatrix} = \begin{bmatrix} L_{11}\mathbf{I}_3 & L_{12}\mathbf{I}_3 & L_{13}\mathbf{I}_3 & L_{14}\mathbf{I}_3 & L_{15}\mathbf{I}_3 & L_{16}\mathbf{I}_3 \\ L_{21}\mathbf{I}_3 & L_{22}\mathbf{I}_3 & L_{23}\mathbf{I}_3 & L_{24}\mathbf{I}_3 & L_{25}\mathbf{I}_3 & l_{26}\mathbf{I}_3 \\ L_{31}\mathbf{I}_3 & L_{32}\mathbf{I}_3 & L_{33}\mathbf{I}_3 & L_{34}\mathbf{I}_3 & L_{35}\mathbf{I}_3 & L_{36}\mathbf{I}_3 \end{bmatrix} \begin{Bmatrix} \mathbf{U}_1 \\ \vdots \\ \mathbf{U}_6 \end{Bmatrix} = \mathbf{B}\mathbf{U}_{1..6} \tag{12}$$

where $\mathbf{L} = [L_{ij}]$ has been defined below Eq.(3); $\mathbf{B}$ and $\mathbf{U}_{1..6}$ are self-defined. Recalling that $\mathbf{B}$ is a constant matrix for each triangle, the internal bending force and tangential bending stiffness required for the nonlinear solution procedure are:

$$\mathbf{f}^b = \frac{\partial E^b}{\partial \mathbf{U}_{1...6}} = A(\mathbf{B}^T\mathbf{D}^b\mathbf{B})\mathbf{U}_{1...6} \ , \quad \mathbf{k}^b = \frac{\partial}{\partial \mathbf{U}_{1...6}}(\frac{\partial E^b}{\partial \mathbf{U}_{1...6}})^T = A(\mathbf{B}^T\mathbf{D}^b\mathbf{B}). \tag{13}$$

The salient feature of the present RF triangle is that the bending energy and its derivatives are independent of $\mathbf{U}^C$ and $\mathbf{n}$. In particular, the tangential bending stiffness matrix is constant and does not require to be updated in the nonlinear solution procedure.

It should be remarked that the "small-curvature" assumption requires the relative curvature defined as nodal spacing divided by the radius of curvature to be small only. In other words, large curvature can be considered by using a small nodal spacing.

2.3. *Membrane formulation by three-node displacement interpolation*

The constant strain triangle (CST) based upon the total Lagrangian framework and three-node displacement interpolation is adopted to take the membrane energy into account. In other words, the constant Green membrane strain is employed which can be expressed as:

$$\mathbf{\varepsilon} = \left\{ \begin{array}{c} \varepsilon_{xx} \\ \varepsilon_{yy} \\ 2\varepsilon_{xy} \end{array} \right\} = \frac{1}{2} \left\{ \begin{array}{c} (\mathbf{X}+\mathbf{U}),_x^T (\mathbf{X}+\mathbf{U}),_x -1 \\ (\mathbf{X}+\mathbf{U}),_y^T (\mathbf{X}+\mathbf{U}),_y -1 \\ 2(\mathbf{X}+\mathbf{U}),_x^T (\mathbf{X}+\mathbf{U}),_y \end{array} \right\} \tag{14}$$

For small strain, the membrane energy can be expressed as:

$$E^m = \frac{A}{2} \mathbf{\varepsilon}^T \mathbf{D}^m \mathbf{\varepsilon} \tag{15}$$

where $\mathbf{D}^m = [D_{ij}^m]$ is the membrane rigidity matrix. The internal membrane force vector and tangential membrane stiffness matrix of the element can be derived by differentiating the membrane energy once and twice with respect to the nodal displacement. Interested readers are referred to [Zhou and Sze, 2012] for the predictions of RFT3 in static shell and drape problems.

2.4. *Explicit time integration for dynamic simulations*

To extend the RFT3 to dynamic simulations, the following equation of motion for a discretized system is first considered:

$$\mathbf{M}\ddot{\mathbf{D}} + \mathbf{F}^{damp} + \mathbf{F} = \mathbf{P} \tag{16}$$

in which $\mathbf{M}$, $\ddot{\mathbf{D}}$, $\mathbf{F}^{damp}$, $\mathbf{F}$ and $\mathbf{P}$ are the mass matrix, acceleration vector, damping force vector, internal force vector and prescribed external force vector, respectively. Among them, $\mathbf{F}$ is assembled from the bending and membrane force vectors of RFT3; the damping force is often a function of the velocity $\dot{\mathbf{D}}$, i.e.

$$\mathbf{F}^{damp} = \mathbf{F}^{damp}(\dot{\mathbf{D}}) . \tag{17}$$

In the explicit time integration, the equation of motion at time t_n is used to obtain the solution after t_n, i.e.

$$\ddot{\mathbf{D}}_n = \mathbf{M}^{-1}(\mathbf{P}_n - \mathbf{F}_n - \mathbf{F}_n^{damp}) \text{ or } \ddot{\mathbf{D}}_n = diag.[\frac{1}{M_{11}}, \frac{1}{M_{22}}, ...](\mathbf{P}_n - \mathbf{F}_n - \mathbf{F}_n^{damp}) \tag{18}$$

The diagonal feature of $\mathbf{M}$ is attained by dividing the mass of each triangle into three and lumped at the three nodes. $\mathbf{F}_n^{damp}$ depends on $\dot{\mathbf{D}}_n$ which is not available. Following the asynchronous damping [Weimar, 2001], $\mathbf{F}_n^{damp}$ is approximated as:

$$\mathbf{F}_n^{damp} = \mathbf{F}^{damp}(\dot{\mathbf{D}}_n) \simeq \mathbf{F}^{damp}(\dot{\mathbf{D}}_{n-1/2}) = \mathbf{F}_{n-1/2}^{damp} . \tag{19}$$

and Eq.(18) is revised as:

$$(a) \ \ddot{\mathbf{D}}_n = diag.[\frac{1}{M_{11}}, \frac{1}{M_{22}}, ...](\mathbf{P}_n - \mathbf{F}_n - \mathbf{F}_{n-1/2}^{damp}) \tag{20}$$

Using the central difference approximation,

$$(b) \ \dot{\mathbf{D}}_{n+1/2} = \dot{\mathbf{D}}_{n-1/2} + \ddot{\mathbf{D}}_n \Delta t \tag{21}$$

$$(c) \ \mathbf{D}_{n+1} = \mathbf{D}_n + \dot{\mathbf{D}}_{n+1/2} \Delta t \tag{22}$$

(a) to (c) form the employed explicit time integration scheme.

3. Six-node interpolation for the membrane strain

Although RFT3 is efficient and performs well in the previous numerical tests [Zhou and Sze, 2012], non-physical sharp folds are sometimes observed in dynamic analyses [Zhou,

2013] and when coarse meshes are employed as shown in Fig. 1. The causes have been traced to be the small-curvature assumption coupled with the membrane energy computed by the CST. As a simple illustration, the initial configuration in Fig. 3(a) is considered in which the nodal spacing is 1 cm. Imagine that nodes 2 to 6 are fixed whilst node 1 moves towards node 4 over 5-6 with the lengths of 1-5 and 1-6 kept unchanged. For the prescribed deformation, the total energy per unit area evaluated at the centroid of 4-5-6 is:

$$E = \frac{1}{2}(D_{11}^b \kappa_{xx}^2 + D_{11}^m \varepsilon_{xx}^2)\big|_{\text{centroid of 4-5-6}}.$$ (23)

Let x be aligned with warp and the wool properties measured by Kang & Yu [1995] be considered, i.e. D_{11}^b = 0.083 gf·cm and D_{11}^m = 1118.2 gf/cm. Fig. 3(b) plots the total energy against the angle ϕ defined by the two chained lines joining node 1, mid-point of 5-6 and node 4, see Fig. 3(a). In the prescribed deformation, ε_{xx} computed by RFT3 vanishes. The figure also plots the total energy in which the bending energy is computed by RFT3 but the membrane energy is computed from the more accurate six-node displacement interpolation. The membrane energy as computed by the six-node displacement interpolation increases significantly as the curvature departs from the small-curvature assumption. Hence, this membrane energy would be a more appropriate companion to the bending energy of the RFT3 than one currently used in RFT3 for suppressing the non-physical sharp folds:

Although one can compute the membrane energy directly from a six-node interpolation, the scheme using the parametric interpolation presented by Flores & Onãte [2005] in their EBST RF triangle appears to be handful and reasonably efficient for boundary treatment. In the scheme, the global coordinate vector **X** and local coordinate vector **x** of the nodes in the initial configuration as well as the displacement are interpolated as:

$$\mathbf{X} = \sum_{i=1}^{6} N_i \mathbf{X}_i \ , \ \ \mathbf{x} = \sum_{i=1}^{6} N_i \mathbf{x}_i \ \text{ and } \ \mathbf{U} = \sum_{i=1}^{6} N_i \mathbf{U}_i$$ (24)
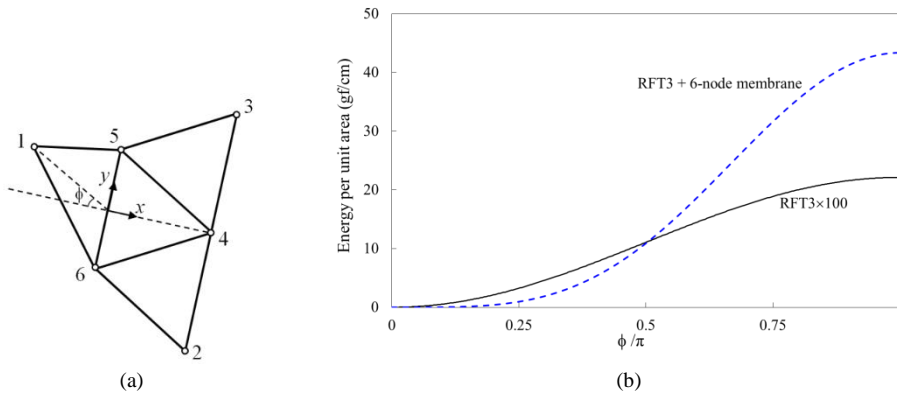

(a)   (b)

Fig. 3. Comparison of the energy at the centroid of 4-5-6 when the membrane energy is considered by three-node and six-node displacement interpolations.

where $N_1=\eta(\eta-1)/2$, $N_2=\zeta(\zeta-1)/2$, $N_3=\xi(\xi-1)/2$, $N_4=\eta+\zeta\xi$, $N_5=\zeta+\xi\eta$, $N_6=\xi+\eta\zeta$ and $\zeta=1-\xi-\eta$. In the interpolation functions, ξ, $\eta \in [-1,+1]$ are the parametric coordinates as shown in Fig. 4(a). Thus, the Green strain in Eq.(14) can be computed accordingly and the following chain rule is required:

$$\begin{Bmatrix} \partial/\partial x \\ \partial/\partial y \end{Bmatrix} = \begin{bmatrix} \partial x/\partial\xi & \partial x/\partial\eta \\ \partial y/\partial\xi & \partial y/\partial\eta \end{bmatrix}^{-1} \begin{Bmatrix} \partial/\partial\xi \\ \partial/\partial\eta \end{Bmatrix} \tag{25}$$

To compute membrane energy in 4-5-6, the strains at I, II and III which are the mid-points of 5-6, 6-4 and 4-5, respectively, are averaged and taken to be the strain within 4-5-6. A one-point quadrature rule can be used accordingly. It can be checked that:

$$\begin{bmatrix} N_{2,\xi} & N_{3,\xi} \\ N_{2,\eta} & N_{3,\eta} \end{bmatrix}_{\xi=1/2,\eta=0} = \begin{bmatrix} N_{3,\xi} & N_{1,\xi} \\ N_{3,\eta} & N_{1,\eta} \end{bmatrix}_{\xi=1/2,\eta=1/2} == \begin{bmatrix} N_{1,\xi} & N_{2,\xi} \\ N_{1,\eta} & N_{2,\eta} \end{bmatrix}_{\xi=0,\eta=1/2} \tag{26}$$

Taking I as an example, the strain at I depends only on the coordinates and displacement of the four nodes bounding I. Similar dependence can be drawn for II and III.

For the boundary treatment, Fig. 4(b) is considered in which A, B and H are the image nodes required to compute the bending energy in RF models [Phaal and Calladine, 1992a; Zhou and Sze, 2012]. To compute the membrane energy of D-E-H, the strains at II, V and VI are required. With the membrane strain at II taken to be the strain obtained by the three-node displacement interpolation of D-E-H, the membrane strain energy would be independent of any image node displacement. Similarly, to compute the membrane energy of C-D-G, the strains at I, III and IV are required. With the membrane strains at I and III taken to be the ones obtained by three-node displacement interpolation of C-D-G, the strain energy would again be independent of any image node displacement.

For convenience, the modified RF model in which a six-node displacement interpolation is employed to take the membrane energy into account is abbreviated as RFT6.
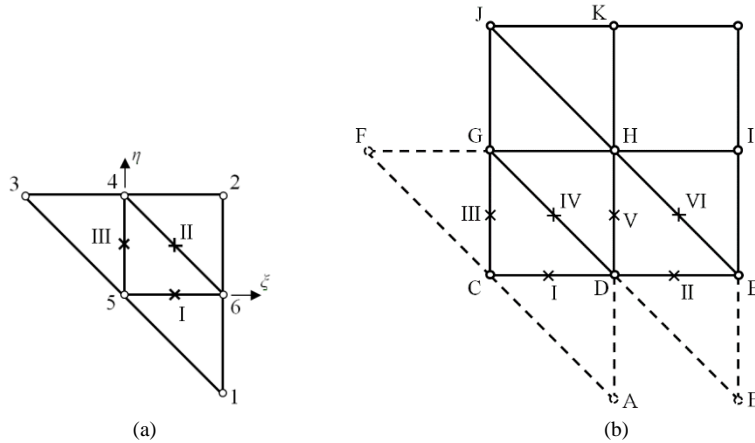

Fig. 4. (a) Element patch in its parametric coordinates system. (b) A typical domain boundary.

4. Examples on Static Drapes

In this section, some of the static drape problems considered by RFT3 in [Zhou and Sze, 2012] are re-considered by RFT6. In all examples, wool fabric with the following properties [Kang and Yu, 1995] is considered:

tensile rigidity along the warp: 1118.2 gf/cm; tensile rigidity along the weft: 759.5 gf/cm;

bending rigidity along the warp: 0.083 gf·cm; bending rigidity along the weft: 0.063 gf·cm;

shear rigidity: 41.8 gf/cm; bending rigidity for the twisting: 0.027 gf·cm;

and the fabric weight: 0.019 gf/cm^2.

To enhance the convergence, the simple scaling scheme for the iterative refinement given in [Liu and Sze, 2009; Zhou and Sze, 2012] is also employed. In all examples, warps and wefts in the initial configuration are always aligned with the global X- and Y- directions.

4.1. *Kang & Yu's example on clamped fabric strip*

In this example, a 1×5 cm strip clamped at one end is draped under its own weight. This example has also been considered in [Kang and Yu, 1995; Teng *et al.*, 1999; Liu and Sze, 2009; Zhou and Sze, 2012]. As shown in Fig. 5, the normalized curvature is small. Thus, the predictions given by RFT3 and RFT6 are almost the same. Both of them agree well with the reference solution yielded by using 10×50 Abaqus S4R elements [Zhou and Sze, 2012].

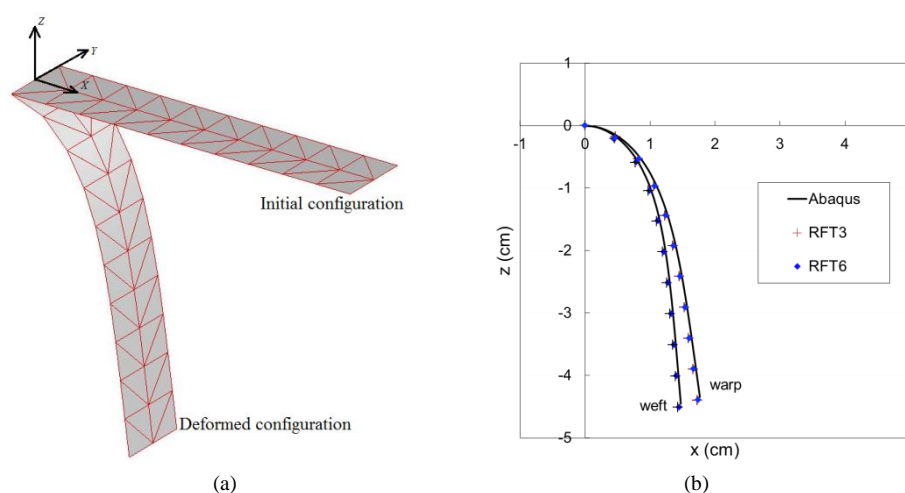(a)   (b)

Fig. 5. Predictions for Kang & Yu's example on a 1×5 cm wool strip clamped at one end. (a) Initial and deformed configurations of the strip; (b) side view of the predictions of RFT3 and RFT6 as well as the reference solution given by Abaqus.
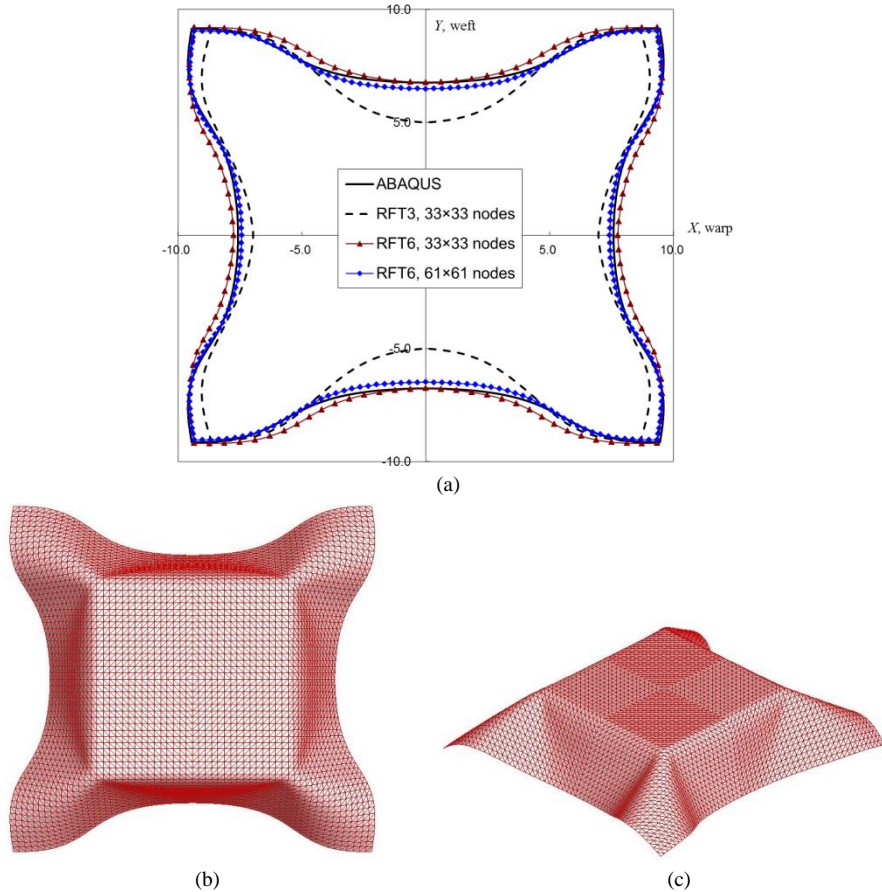
(a)

(b)   (c)

Fig. 6. Predictions for Kang & Yu's example on a 20×20 cm fabric draped over on a 10×10 cm pedestal. (a) The deformed boundary predicted by Abaqus, RFT3 and RFT6; (b) Top and (c) isometric views predicted by RFT6 using 61×61 nodes.

4.2. *Kang & Yu's example on a square cloth draped on a square pedestal*

In this example, a 20×20 cm fabric is draped over a 10×10 cm square pedestal. Kang & Yu [1995] conducted the physical experiment for this example and the measured result is often used to qualitatively compare with predictions from drape simulations [Kang and Yu, 1995; Teng *et al.*, 1999; Liu and Sze, 2009; Zhou and Sze, 2012]. Nevertheless, the measured configuration is not symmetric which might be caused by various environmental and human factors. Here, a highly converged solution with respect to the mesh density obtained by 120×120 Abaqus S4R shell elements in [Zhou and Sze, 2012] is employed as the reference solution. Fig. 6(a) shows the top views of the fabric boundaries predicted by RFT3 and RFT6. Using 33×33 nodes, the RFT3 is too flexible, especially in the weft direction, whilst RFT6 is too stiff. However, the prediction of RFT6 is much closer to the reference solution. It can also been seen that RFT6 yields a

better prediction when 61×61 nodes are employed. The related top and isometric views are plotted in Fig. 6(b) and (c), respectively. Both of them look realistic.

4.3. *Square fabric draped on square pedestals with long free-hanging lengths*

Fig. 7 shows a 40×40 cm fabric draped over a 20×20 cm pedestal predicted by RFT6 with 81×81 nodes. The prediction of RFT3 appears to be very similar and, thus, is not here repeated to save space. A 80×80 cm fabric draped over a 40×40 cm pedestal is then considered with again 81×81 nodes. Figs. 8(a)-(b) show the prediction of RFT3 whilst Figs. 8(c)-(d) show the prediction of RFT6. In this example, the prediction of RFT3 is less stiff than that of RFT6. Both sets of predictions look realistic and match our daily perception. However, the enlarged views in Figs. 8(e)-(f) for the predictions of RFT3 and RFT6, respectively, reveal that non-physical sharp folds have been developed in the prediction of the RFT3 but not RFT6. That is the underlining reason for the related "softer" look.

4.4. *A square cloth draped on a circular pedestals*

RFT3 and RFT6 are further compared by using a relatively coarse unstructured mesh with 371 nodes and 646 triangles to model a 50×50 cm fabric draped over a Ø20 cm pedestal. The prediction of RFT3 has been portrayed in Fig. 1 and possesses many non-physical sharp folds. On the other hand, the prediction of RFT6 in Fig. 9 is smooth and contains no sharp fold. The slight asymmetry is inherit from that of the mesh. Next, we will illustrate that the mesh density is not adequate to resolve finer details of the deformed configuration.

The same fabric sheet is modelled with 21×160 and 31×240 nodes. The predictions of RFT6 are portrayed in Figs. 10(a)-(b) and 10(c)-(d), respectively. The two sets of predictions look similar and 12 folds are observed, indicating that the mesh with 21×160 nodes has been adequate. They also agree well with those of RFT3 in [Zhou and Sze, 2012].
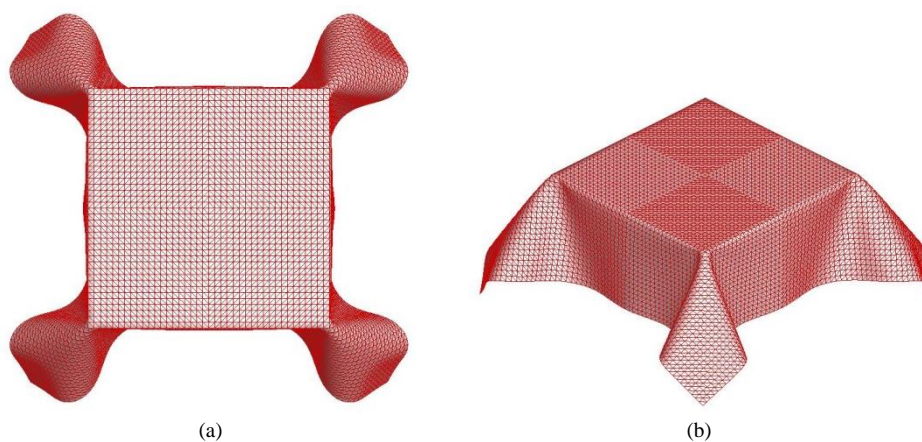

(a)   (b)

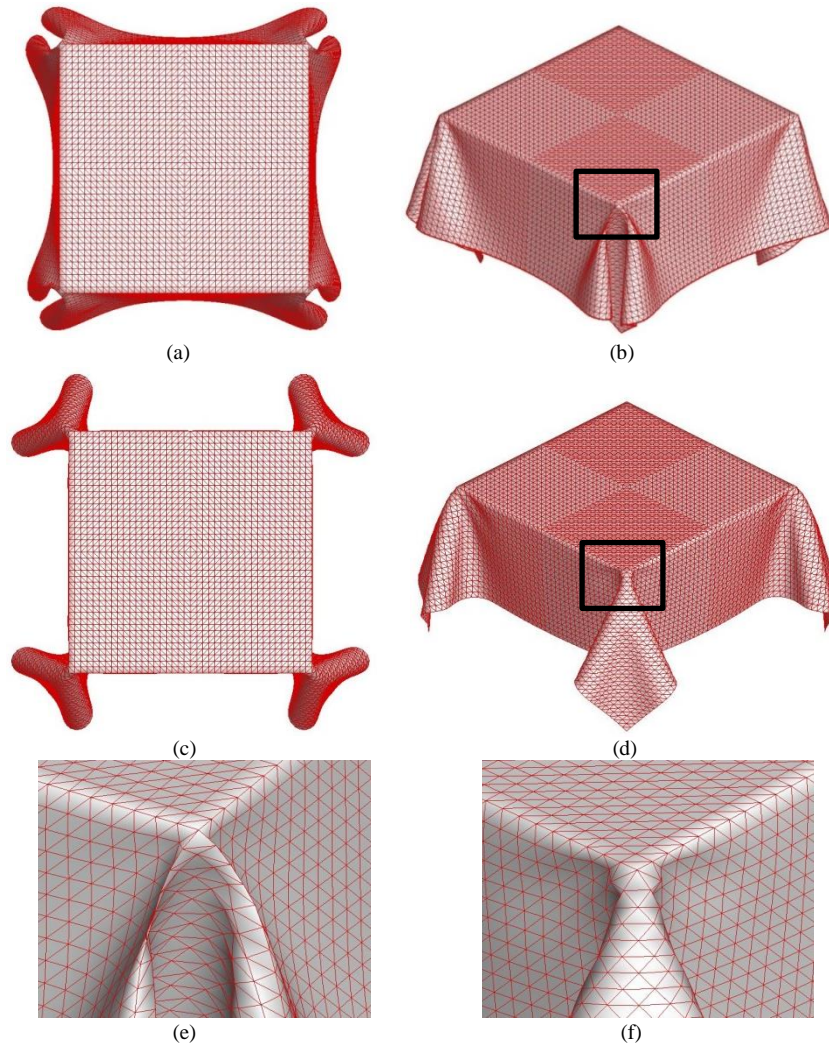Fig. 7. A 40×40 cm fabric draped over a 20×20 cm pedestal. (a) Top and (b) isometric views predicted by RFT6 using 81×81 nodes.

Fig. 8. A 80×80 cm fabric draped over a 40×40 cm pedestal modelled by 81×81 nodes. (a) Top and (b) isometric views predicted by RFT3. (c) Top and (d) isometric views predicted by RFT6. (e) and (f) are the enlarged viewed of the boxed regions in (b) and (d), respectively.

4.5. *A square cloth draped on a sphere*

In this example, a 30×30 cm square cloth is draped over a Ø10 cm sphere. As the spherical surface can be expressed in a simple mathematic expression, the contact can be conveniently handled by the penalty method as in [Liu and Sze, 2009; Zhou and Sze, 2012]. The prediction of RFT6 by using 61×61 nodes are shown in Figs. 11(a)-(b). They look nature and are also consistent with the predictions of RFT3 in [Zhou and Sze, 2012].
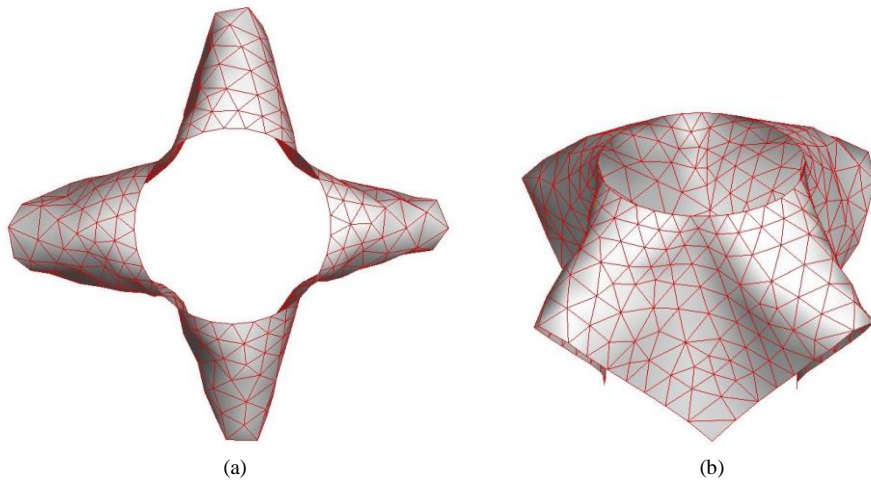
Fig. 9. (a) Top and (b) isometric views of a 50×50 cm fabric on a Ø20 cm pedestal predicted by RFT6 using 371 nodes.
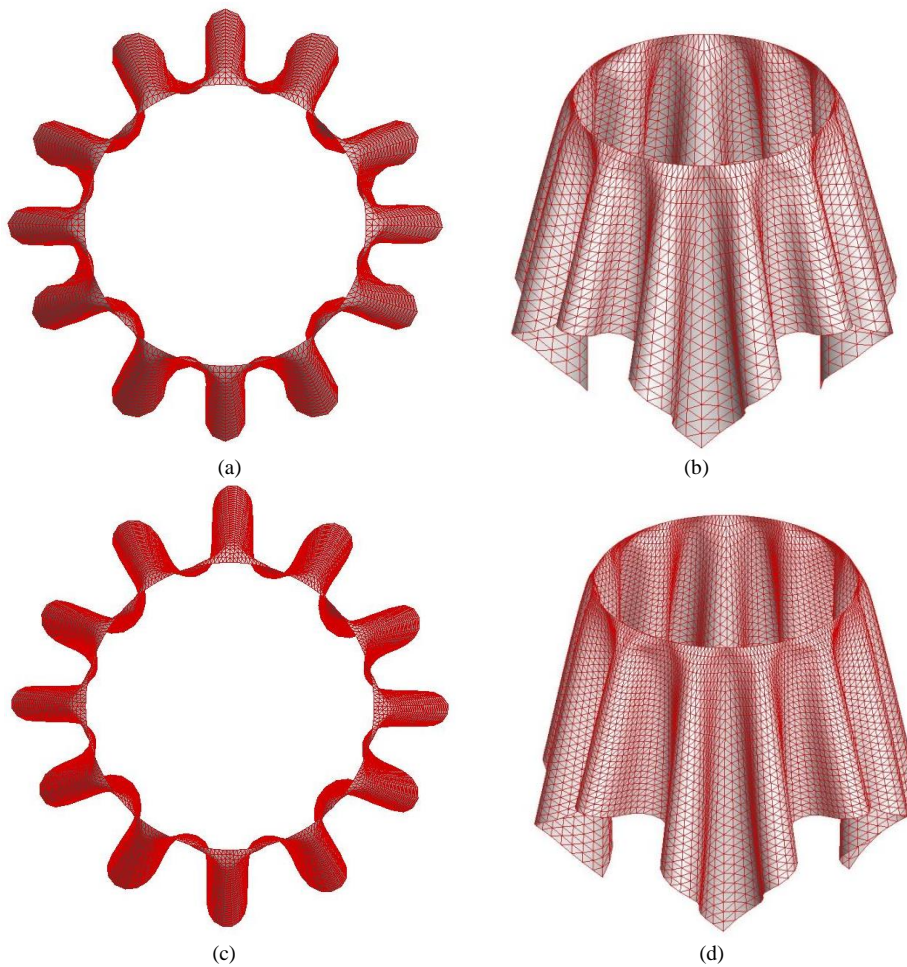

Fig. 10. A 50×50 cm fabric draped over a Ø20 cm pedestal. (a) Top and (b) isometric views predicted by using 21×160 nodes; (c) top and (d) isometric views predicted by using 31×240 nodes.

When a coarser mesh with only 17×17 nodes is employed, the prediction of RFT6 is shown in Figs. 11(c)-(d). Although the fabric appears to be a bit stiffer, the draped pattern still looks smooth and nature. On the other hand, RFT3 fails to converge. In the un-converged solution, non-physical sharp folds and self-penetrations of the fabric sheet are noted.

The important message conveyed in the last two and present examples is that RFT6 is more capable of producing smooth and realistic predictions than RFT.

4.6. *Dynamic draping of square fabrics hanged at two corners*

To demonstrate the dynamic simulation, draping of two square fabric sheets of side lengths 20 and 100 cm are considered. They are modelled by 41×41 and 51×51 nodes as shown in Figs. 12(a) and 13(a), respectively. Initially, they are kept flat, horizontal and stress-free. With the two adjacent corners pinned, they are then allowed to fall under gravity at $t = 0$. A viscous mass damping is introduced in these examples, and the damping force in Eq.(17) is expressed as:

$$\mathbf{F}^{damp} = -\alpha \mathbf{M} \dot{\mathbf{D}} \tag{27}$$

in which the mass damping factor α is set rather arbitrarily and empirically to be 5.0 sec^{-1}. Mass damping is considered to be reasonable for air resistance which increases with the

<div align="center">(a)</div>

<div align="center">(b)</div>

<div align="center">(c)</div>

<div align="center">(d)</div>
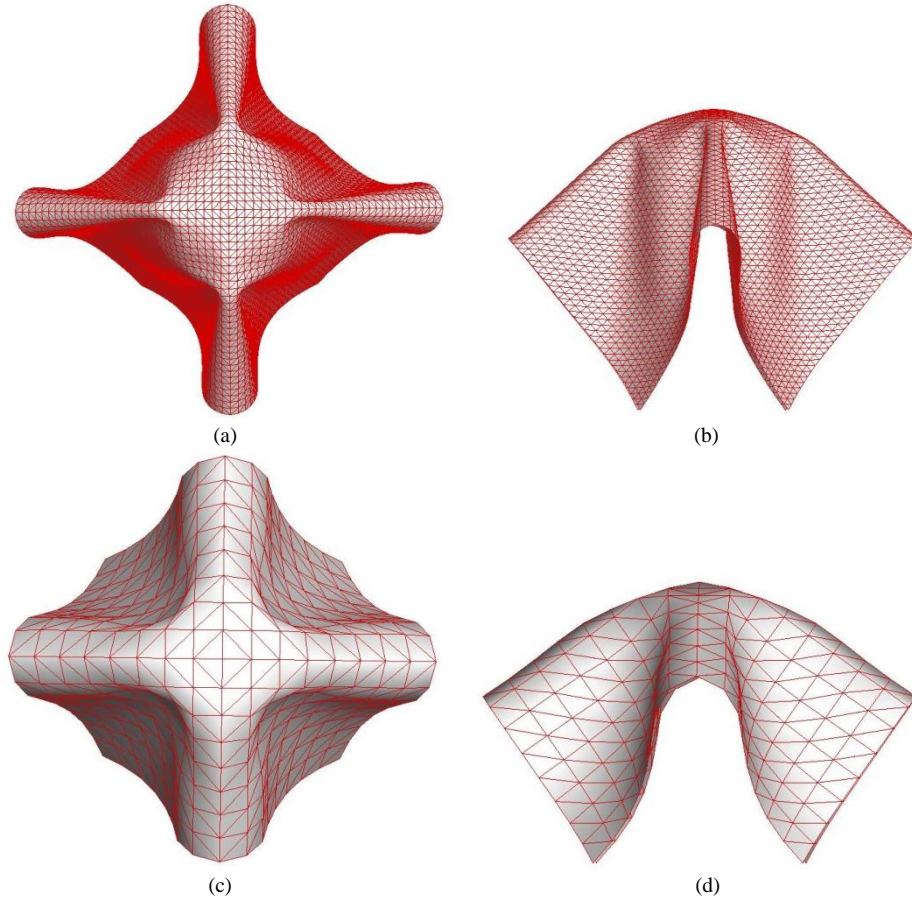
Fig. 11. A square fabric drapes over a sphere. (a) Top and (b) side views predicted by using 61×61 nodes. (c) Top and (d) side views predicted by using 17×17 nodes.

surface area. Fig. 12 extracts the frames showing smaller sheet at $t = 0$, 0.16, 0.32 and 2 seconds. At $t = 2$ seconds, the fabric sheet has basically stop moving. Fig. 13 extracts the frames showing the larger sheet at $t = 0$, 0.48, 1.44 and 2.4 seconds. At $t = 2.4$ seconds, the larger sheet has basically stop moving. Comparing their transient and steady-state configurations, it can be seen that the small sheet overshoot its steady-state configuration more significantly than the larger sheet. On the other hand, the latter falls more slowly and the steady-state configuration shows more wrinkles than the former. The transient and steady-state configurations look realistic. Interested readers can download the related zipped Flash movies at http://1drv.ms/1gHS8HX.
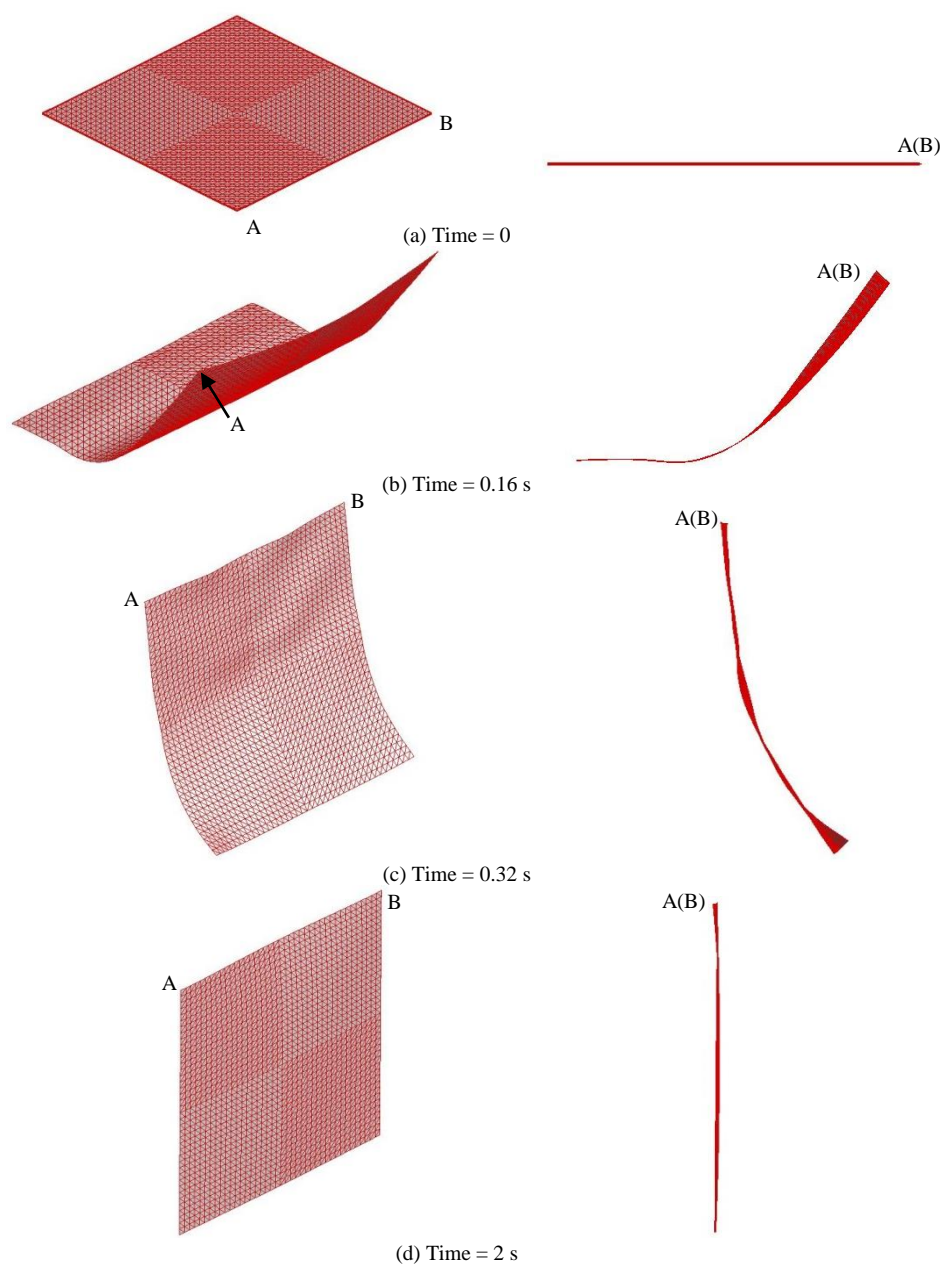
(a) Time = 0

(b) Time = 0.16 s

(c) Time = 0.32 s

(d) Time = 2 s

Fig. 12. Dynamic draping of a 20×20 cm square fabric hanged at the two adjacent corners. (a) to (d) are isometric and side views at different instants.

(a) Time = 0

(b) Time = 0.48 s
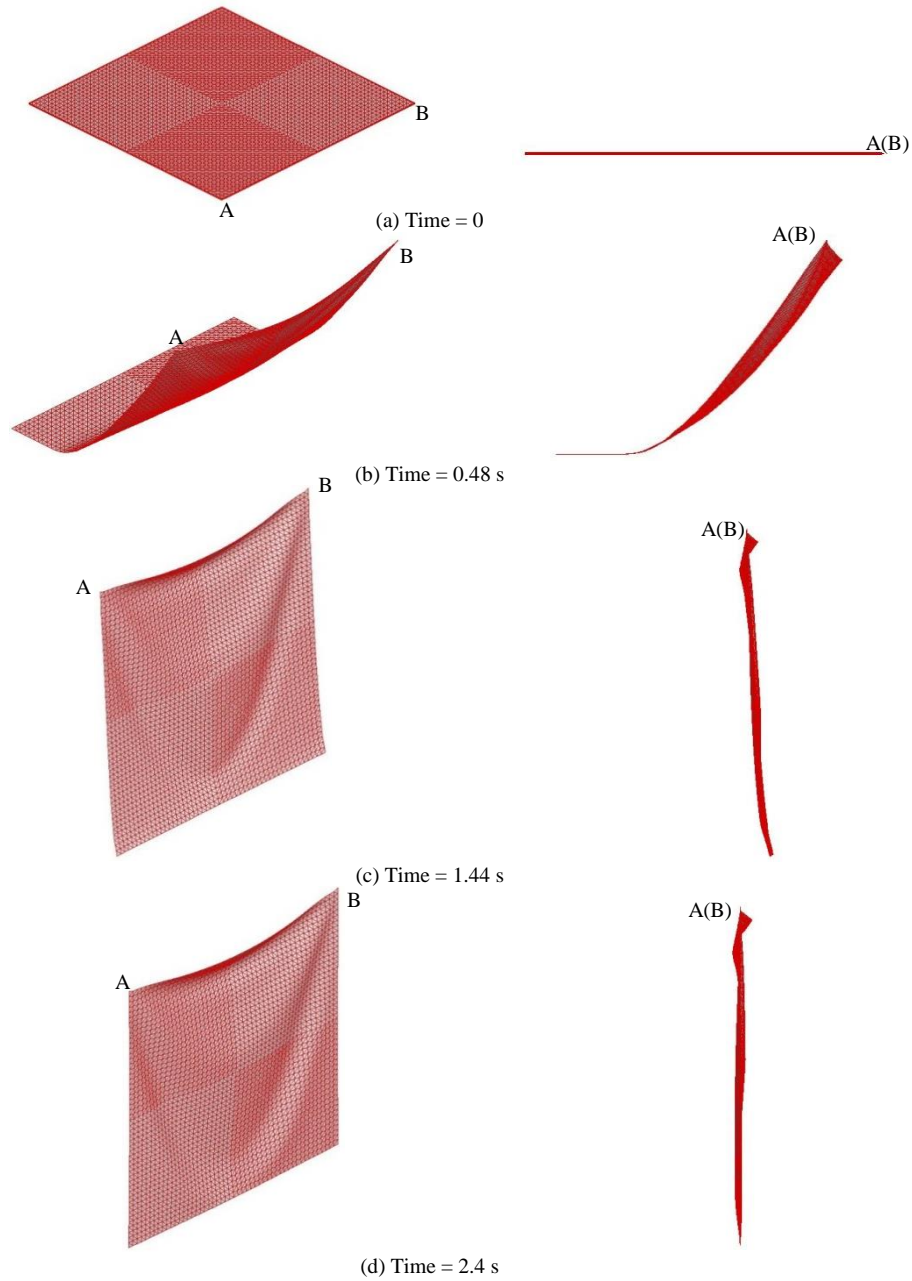
(c) Time = 1.44 s

(d) Time = 2.4 s

Fig. 13. Dynamic draping of a 100×100 cm square fabric hanged at the two adjacent corners. (a) to (d) are isometric and side views at different instants.

5. Adaptive Remeshing

Sections 4.3, 4.4 and 4.6 show that new membrane formulation in RFT6 is effective to suppress the non-physical sharp fold and more able to deliver smooth realistic predictions

than RFT3. Section 4.4 also illustrates that the absence of sharp fold does not necessary imply an adequate nodal density. To secure an adequate but not excessive nodal density, adaptive remeshing has been a popular technique. It can also avoid large relative curvature and, thus, the deviation of the small-curvature assumption in the bending model.

Several adaptive remeshing schemes have been proposed for drape/cloth simulations, see [Zhang and Yuen, 2001; Villard and Boeouchaki, 2005; Volkov and Li, 2005; Narain *et al.*, 2012], for instances. Most of them are based on the local remeshing/refinement which may sometimes cause poor mesh qualities especially for the regions close to the domain boundaries and/or between different hierarchical levels. Furthermore, these schemes usually require adaptive data structures and add complexity to the implementation [Narain *et al.*, 2012]. These drawbacks are particularly valid for RF models as the interpolation domain is larger than the integration domain and remeshing in one element requires the interpolation domains of the neighbouring elements be changed. On the other hand, the global adaptive remeshing commonly used in structural analyses is seldom seen in drape/cloth simulations. The major reason is probably that the bending rigidity of fabric is very weak. The transfer from the old to an entirely new mesh often causes considerable oscillation which adversely affects the simulation quality. However, if only the steady-state configuration is concerned as in the dynamic relaxation method, the global adaptive remeshing can be a good choice for achieving high-quality meshes for capturing folds/wrinkles. In this work, the global adaptive refinement scheme of Lee & Lo [1995] will be generalized to dynamic drape simulations, and further to garment sewing simulations in Part II of the present series. The advancing front technique [Lo and Lee, 1994] is employed to generate the mesh and the interpolation domain in the RF triangle can be easily traced along with the moving front.

5.1. *Determination of the element size*

In most global adaptive remeshing schemes, the new element sizes are designed by using error indicator and equal error distribution criterion [Lee and Lo, 1995]. However, the related treatments are complex and also unnecessary in drape/cloth simulations which often, if not always, aim at predictions consistent to our daily perception.

Curvature-based expressions are the most commonly used refinement criteria for drape/cloth simulations [Villard and Boeouchaki, 2005; Volkov and Li, 2005; Narain *et al.*, 2012]. Volkov & Li [2005] compared a number of curvature-based criteria and recommended:

$$|\kappa| h^2 > \text{'a prescribed value'} \qquad (28)$$

as the criterion to determine whether local mesh refinement is required. In this expression, h is the element size which will here be taken as the average side length of the RF triangle for simplicity. In global adaptive remeshing, remeshing is conducted for the entire problem domain and the spatial distribution of the targeted element size h_{target} is required. In analogous to Eq.(28), h_{target} is determined from:

$$\left|\mathbf{\kappa}\right|h_{\text{new}}^2 = const \quad \text{and} \quad h_{\text{target}} = \begin{cases} h_{\text{upper}} & \text{for } h_{\text{new}} > h_{\text{upper}} \\ h_{\text{lower}} & \text{for } h_{\text{new}} < h_{\text{lower}} \\ h_{\text{new}} & \text{otherwise} \end{cases} \quad (29)$$

where *const* is a preset coefficient and $\mathbf{\kappa}$ is the curvature vector which can be computed by Eq.(7) for each RF triangle. When the fabric is locally flat or close to flat, the determined h_{target} would be unrealistically large. On the other hand, if the determined h_{target} is too small, stable time step size of the explicit time integration would be unrealistically small. Hence, lower and upper bounds are imposed on h_{target}. A point of remark is that the relative curvature $|\mathbf{\kappa}|h$ is non-dimensional. The additional h in $|\mathbf{\kappa}|h^2$, however, is effective in smoothing the spatial distribution of h_{target} [Volkov and Li, 2005] and this point is echoed in our computational trials.

5.2. *Adaptive remeshing procedure*

The simple yet reliable remeshing scheme of Lee & Lo [1995] is employed. A background grid is used to transfer the element size and kinematic variables (i.e. displacement and velocity) during the adaptive remeshing. The procedures for the adaptive remeshing and advancement of the predictions are summarized below:

    a.   An initial mesh is inputted or generated.

    b.   Form a square background grid covering the initial computational domain for transferring the element sizes and the kinematic variables as in [Lee and Lo, 1995].

    c.   If the existing time step size leads to instability, stop, reduce the integration time step size and restart.

    d.   The time integration is advanced for a prescribed number of time steps. Alternatively, the time integration can be kept advancing until $|\mathbf{\kappa}|h^2$ is larger than a predefined value.

    e.   For each RF triangle in the present mesh, h_{target} is calculated according to Eq.(29).

    f.   Transfer h_{target} and the kinematic variables from the existing mesh to the background grid.

    g.   Use the advancing front technique [Lo and Lee, 1994] to generate a new mesh based on h_{target} stored on the background grid.

    h.   Transfer the kinematic variables from the background grid to the nodes in the new mesh.

    i.   Goto *step b*.

6. Numerical examples on Adaptive Remeshing

In this section, three previous static drape problems are re-considered by RFT6 with adaptive remeshing in the dynamic relaxation process. The viscous mass damping in Eq.(27) is again employed and the fabric sheet would finally come to still. As only the static equilibrium configuration is the concern, the mass scaling method is employed to lengthen the stable time step and reduce the fictitious oscillation during remeshing. Here,

the mass matrix is scaled up 100 times. The weight in the external force vector is kept unchanged. Flash movies for the examples in this section showing the remeshing along with the dynamic relaxation can be downloaded at http://1drv.ms/1gHS8HX.
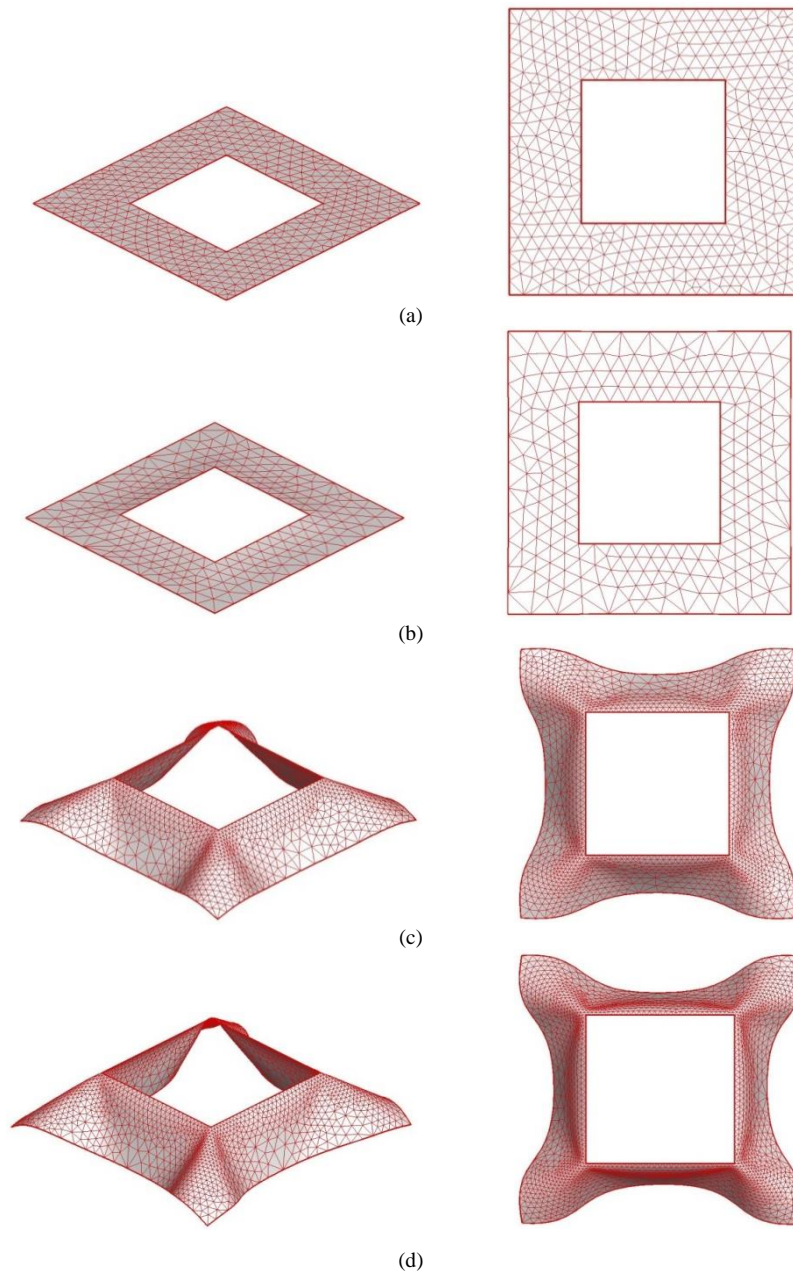

(a)

(b)

(c)

(d)

Fig. 14. Kang and Yu's example on a 20×20 cm cloth draped over a 10×10 cm square pedestal. (a) to (d) are isometric and top views at different instants.

6.1. *Kang & Yu's example on a square cloth draped on a square pedestal*

Fig. 14 shows the representative frames for the 20×20 cm fabric sheet which has also been considered in Section 4.3. The computation starts with the unstructured mesh in Fig. 14(a). At the very beginning, the curvature is small and the remeshed mesh gets coarser as shown in Figs. 14(a)-(b). Once larger and larger curvature comes in, the mesh is successively refined as shown in Figs. 14(b)-(d). Comparing Fig. 5 with Fig. 14(d), one can see that the static drape yielded by the iterative static equilibrium solution and the dynamic relaxation are highly similar.

6.2. *A square cloth draped on a circular pedestals*

Fig. 15 shows the representative frames for the 50×50 cm square fabric draped on a Ø20cm pedestal. When the adaptive remeshing is employed along with the dynamic relaxation, the final configuration in Fig. 15(d) is attained. Although the prediction possesses 8 folds whist 12 folds are predicted in the iterative static equilibrium solution portrayed in Fig. 10 by using a dense structural mesh, both predictions look realistic. It is not surprising to see two solutions as drape problems can possess multiple solutions [Liu and Sze, 2009] and different solution schemes can converge to different solutions.

6.3. *A square cloth draped on a sphere*

Fig. 16 shows the representative frames of a 30×30 cm fabric draped on a Ø10 cm sphere. For the contact treatment, the kinematic constraint commonly used in dynamic simulations is employed to replace the penalty method used in Section 4.5 for the contact treatment. If penetration occurs at the end of a time step, a radial displacement correction will be applied to the penetrated node such that it would rest on the surface of the sphere and the corrected displacement is treated as the displacement solution at the end of the time step. Starting with the coarse initial mesh in Fig. 16(a), realistic prediction for the steady-state drape in Fig. 16(d) with high quality mesh is obtained. The drape pattern is largely consistent with that in Fig. 11 which portrays the iterative static equilibrium solution.

7. Closure

In this paper, the non-physical sharp folds which sometimes appear in the intermediate and converged solutions of the previous rotation-free triangle RFT3 are subdued by computing the membrane strain from the six-node instead of the three-node displacement interpolation. By applying the modified rotation-free triangle RFT6 to drape simulations, the yielded predictions are essential the same as those of RFT3 when the meshes are dense. When the meshes are coarse, the non-physical sharp folds appear in the predictions of RFT3 are largely suppressed in those of RFT6. Furthermore, a global adaptive remeshing capability is developed by using the advancing front method. The element size in the new mesh is controlled by curvature prediction of the old mesh. Numerical examples demonstrate that the remeshing scheme along with the dynamic

relaxation method can provide sufficient mesh density to capture the realistic folds in drape simulations.

In the second paper of this series, some techniques from computer graphics and textile engineering, e.g., collision detection and treatment, human body model construction and garment sewing, will be introduced and integrated with the RFT6. Simulation of clothes on still and moving human body model will be presented.
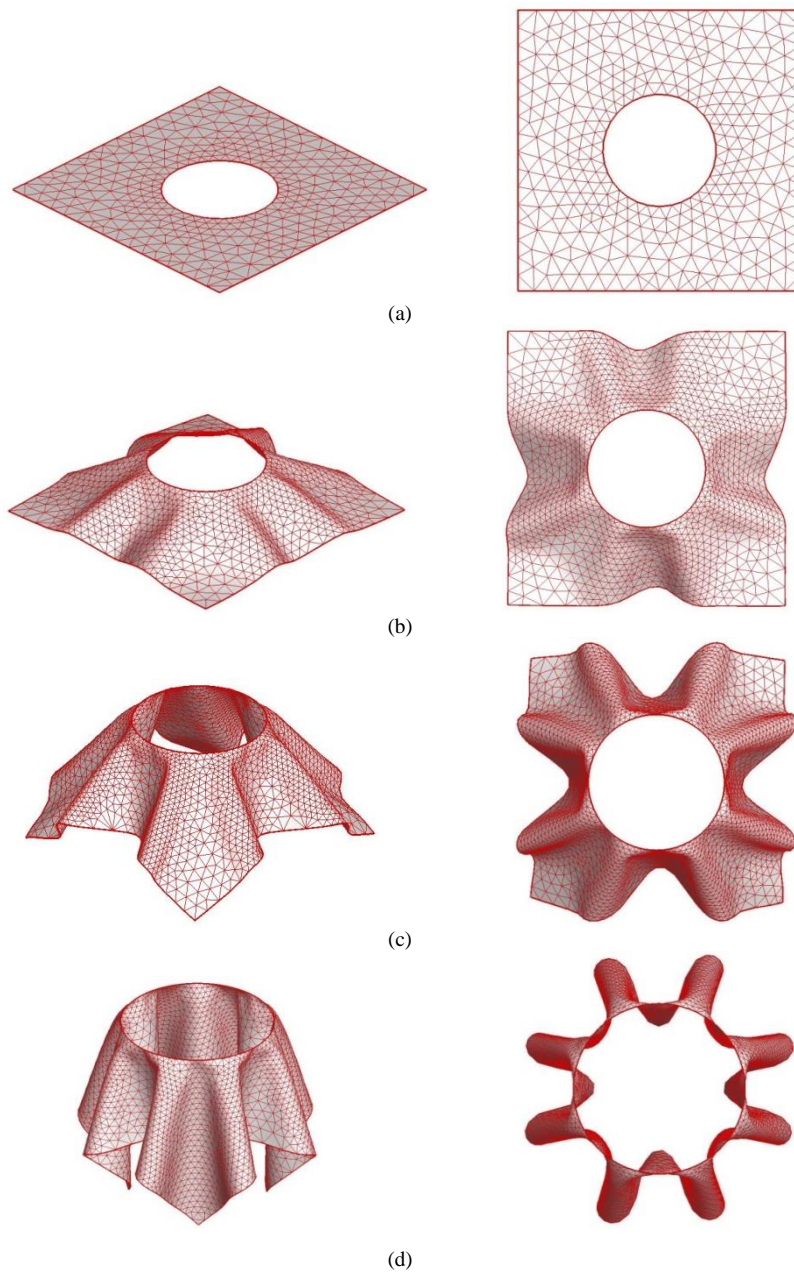

(a)

(b)

(c)

(d)

Fig. 15. A 50×50 cm cloth draped over a Ø20 cm pedestal. (a) to (d) are isometric and top views at different instants.
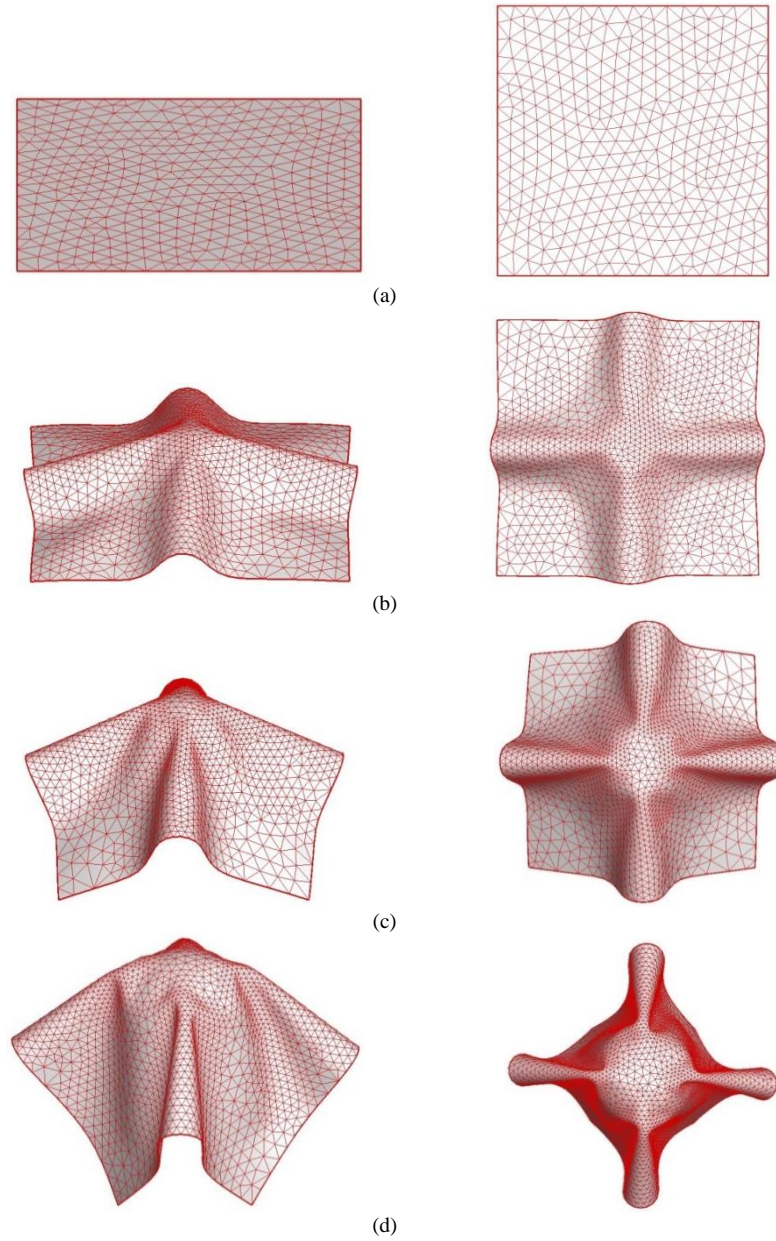
Fig. 16. A square cloth draped over a sphere. (a) to (d) are isometric and top views at different instants

Acknowledgments

References

Benson, D.J., Bazilevs, Y., Hsu, M.C., and Hughes, T.J.R. [2011]. A large deformation, rotation-free, isogeometric shell. *Comput. Methods Appl. Mech. Engrg.,* **200**, 1367-1378.

Breen, D.E., House, D.H., and Wozny, M.J. [1994]. Predicting the drape of woven cloth using interacting particles. *Proc. SIGGRAPH '94*, 365-372.

Chen, S.F., Hu, J.L., and Teng, J.G. [2001]. A finite-volume method for contact drape simulation of woven fabrics and garments. *Finite Elem. Anal. Des.,* **37**, 513-531.

Choi, K.J., and Ko, H.S. [2005]. Research problems in clothing simulaion. *Comput.-Aided Des.,* **37**, 585-592.

Cirak, F., and Ortiz, M. [2001]. Fully C1-conforming subdivision elements for finite deformation thin-shell analysis. *Inter. J. Numer. Methods Engrg.,* **51**, 813-833.

Cui, X.Y., Liu, G.R., Li, G.Y., and Zhang, G.Y. [2011]. A thin plate formulation without rotation DOFs based on the radial point interpolation method and triangular cells. *Inter. J. Numer. Methods Engrg.,* **85**, 958-986.

Eischen, J.W., Deng, S.G., and Clapp, T.G. [1996]. Finite-element modeling and control of flexible fabric parts. *IEEE Comput. Graph. ,* **16**, 71-80.

Flores, F.G., and Onate, E. [2005]. Improvements in the membrane behaviour of the three node rotation-free BST shell triangle using an assumed strain approach. *Comput. Method. Appl. Mech. Engrg.,* **194**, 907-932.

Flores, F.G., and Onate, E. [2011]. Wrinkling and folding analysis of elastic membranes using an enhanced rotation-free thin shell triangular element. *Finite Elem. Anal. Des.,* **47**, 982-990.

Gan, L., Ly, N.G., and Steven, G.P. [1995]. A study of fabric deformation using nonlinear finite elements. *Text. Res. J. ,* **65**, 660-668.

Gardsback, M., and Tibert, G. [2007]. A comparison of rotation-free triangular shell elements for unstructured meshes. *Comput. Method. Appl. Mech. Engrg.,* **196**, 5001-5015.

Gong, D.X., Hinds, B.K., and McCartney, J. [2001]. Progress towards effective garment CAD. *Inter. J. Cloth. Sci. Tech.,* **13**, 12-22.

Guo, Y., Gati, W., Naceur, H., and Batoz, J. [2002]. An efficient DKT rotation free shell element for springback simulation in sheet metal forming. *Comput. Struct.,* **80**, 2299-2312.

Smith Micro Software Inc. [2012]. *Poser 9 Reference Manual*. Columbia,USA.

Ji, F., Li, R.Q., and Qiu, Y.P. [2006]. Three-dimensional garment simulation based on a spring-mass system. *Text. Res. J.,* **76**, 12-17.

Kang, T.J., and Yu, W.R. [1995]. Drape simulation of woven fabric by using the finite-element method. *J. Text. I.,* **86**, 635-648.

Lee, C.K., and Lo, S.H. [1995]. An automatic adaptive refinement procedure using triangular and quadrilateral meshes. *Eng. Fract. Mech.,* **50**, 671-686.

Liu, X.H., and Sze, K.Y. [2009]. A corotational interpolatory model for fabric drape simulation. *Inter. J. Numer. Methods Engrg.,* **77**, 799-823.

Lo, S.H., and Lee, C.K. [1994]. Generation of gradation meshes by the background grid technique. *Comput. Struct.,* **50**, 21-32.

Narain, R., Samii, A., and O'Brien, J.F. [2012]. Adaptive anisotropic remeshing for cloth simulation. *ACM T. Graphic.,* **31**, Article: 152.

Onate, E., and Zarate, F. [2000]. Rotation-free triangular plate and shell elements. *Inter. J. Numer. Methods Engrg.,* **47**, 557-603.

Phaal, R., and Calladine, C.R. [1992a]. A simple class of finite elements for plate and shell problems. I: Elements for beams and thin flat plates. *Inter. J. Numer. Methods Engrg.,* **35**, 955-977.

Phaal, R., and Calladine, C.R. [1992b]. A simple class of finite elements for plate and shell problems. II: an element for thin shells, with only translational degrees of freedom. *Inter. J. Numer. Methods Engrg.,* **35**, 979-996.

Provot, X. [1995]. Deformation constraints in a mass-spring model to desctibe rigid cloth behavior. *Proc. Graph. Interface*, 147-154.

Sabourin, F., and Brunet, M. [2006]. Detailed formulation of the rotation-free triangular element "S3" for general purpose shell analysis. *Eng. Computation.,* **23**, 469-502.

Sze, K.Y., Chen, J.S., Sheng, N., and Liu, X.H. [2004]. Stabilized conforming nodal integration: exactness and variational justification. *Finite Elem. Anal. Des.,* **41**, 147-171.

Sze, K.Y., and Liu, X.H. [2005]. A new skeletal model for fabric drapes. *Inter. J. Mech. Mater. Des. ,* **2**, 225-243.

Sze, K.Y., and Liu, X.H. [2007]. Fabric drape simulation by solid-shell finite element method. *Finite Elem. Anal. Des.,* **43**, 819-838.

Tan, S.T., Wong, T.N., Zhao, Y.F., and Chen, W.J. [1999]. A constrained finite element method for modeling cloth deformation. *Visual Comput.,* **15**, 90-99.

Teng, J.G., Chen, S.F., and Hu, J.L. [1999]. A finite-volume method for deformation analysis of woven fabrics. *Inter. J. Numer. Methods Engrg.,* **46**, 2061-2098.

Villard, J., and Boeouchaki, H. [2005]. Adaptive meshing for cloth animation. *Eng. Comput.,* **20**, 333-341.

Volino, P., and Cordier, F. [2004]. Cloth simulation. In N. Magnenat-Thalmann & D. Magnenat-Thalmann (Eds.), *Handbook of Virtual Humans*. Chichester: John Wiley & Sons, Ltd.

Volkov, V., and Li, L. [2005]. Adaptive triangular meshes for cloth simulation. *Res. J. Text. Apparel,* **9**(1), 48-59.

Weimar, K. [2001]. LS-DYNA User's Guider. *CAD-FEM GmbH, Munchen*.

Zhang, D.L., and Yuen, M.M.F. [2001]. Cloth simulation using multilevel meshes. *Comput. Graphic.,* **25**, 383-389.

Zhou, Y.X. [2013]. *An efficient rotation-free triangle and its application in cloth simulations.* (PhD thesis), The University of Hong Kong, Hong Kong.

Zhou, Y.X., and Sze, K.Y. [2012]. A geometric nonlinear rotation-free triangle & its application in drape Simulation. *Inter. J. Numer. Methods Engrg.,* **89**(4), 509-536.

Zulch, G., Koruca, H.I., and Borkircher, M. [2011]. Simulation-supported change process for product customization - A case study in a garment company. *Comput. Ind.,* **62**, 568-577.